Effect of Microstructure on the Thermal Conductivity of Plasma Sprayed Y_2O_3 Stabilized Zirconia (8% YSZ)

Ningning Hu [1,2], Matiullah Khan [2,3], Yongzhe Wang [2], Xuemei Song [2], Chucheng Lin [2], Chengkang Chang [1] and Yi Zeng [2,*]

[1]   School of Materials Science and Engineering, Shanghai Institute of Technology, Shanghai 201418, China; ningnhu@163.com (N.H.); ckchang@sit.edu.cn (C.C.)
[2]   The State Key Lab of High Performance Ceramics and Superfine Microstructure, Shanghai Institute of Ceramics, Chinese Academy of Sciences, Shanghai 200050, China; matiullahustb@gmail.com (M.K.); wangyongzhe@mail.sic.ac.cn (Y.W.); songxuemei@mail.sic.ac.cn (X.S.); chucheng@mail.sic.ac.cn (C.L.)
[3]   Department of Physics, Kohat University of Science and Technology, Kohat 26000, Pakistan
*   Correspondence: zengyi@mail.sic.ac.cn; Tel.: +86-21-5241-2107

Abstract: In this paper, the effect of microstructure on the thermal conductivity of plasma-sprayed Y_2O_3 stabilized ZrO_2 (YSZ) thermal barrier coatings (TBCs) is investigated. Nine freestanding samples deposited on aluminum alloys are studied. Cross-section morphology such as pores, cracks, m-phase content, grain boundary density of the coated samples are examined by scanning electron microscopy (SEM) and electron back-scattered diffraction (EBSD). Multiple linear regressions are used to develop quantitative models that describe the relationship between the particle parameters, m-phase content and features of the microstructure such as porosity, crack-porosity, and the length density of small and big angle-cracks. Moreover, the relationship between the microstructure and thermal conductivity is investigated. Results reveal that the thermal conductivity of the coating is mainly determined by the microstructure and grain boundary density at room temperature (25 °C), and by the length density of big-angle-crack, monoclinic phase content and grain boundary density at high temperature (1200 °C).

1. Introduction

Yttria-stabilized zirconia (YSZ) is widely used to protect high-temperature components from corrosion and improve the operating temperature of gas-turbine engines. The main aim is to reduce the thermal conductivity of engine components by using YSZ material prepared by the atmospheric plasma spray (APS) method [1,2]. The spraying parameters and deposition efficiency in the plasma process produce a variety of microscopic defects, with pores and cracks appearing in the coatings [3–5]. These microscopic defects have great influence on the thermal conductivity of TBCs [6].

Recently, advanced instrumentations have made it possible to observe and measure the movement of particles in the spray state [7,8] and determine the velocity and temperature of in-flight particles in air plasma spraying. Many researchers have studied the relationship between the thermal conductivity and the microstructure. Studies show that cracks parallel to the direction of the matrix and pores can effectively reduce the thermal conductivity, while cracks vertical to the direction of the matrix increase the heat transfer [9–11]. The amount of different phase contents of the TBCs has a varying impact on the thermal conductivity. The thermal conductivity of monoclinic zirconia is higher than that of the tetragonal and cubic phases [11–13]. Some studies have investigated the relationship between the spray process and the microstructure of the thermal barrier coating. It was found that,

with increasing particle velocity and temperature, the coating is densified and the thermal conductivity increases [14,15]. The quantitative effect of grain boundaries on the thermal conductivity was analyzed, showing that the thermal conductivity of small grains is lower than that of large grains [16–18].

Unfortunately, most studies have focused on the qualitative effect of microstructure on the thermal conductivity in the thermal barrier coating [19–21]. Nevertheless, very limited literature on the quantitative relationship between the microstructure and thermal conductivity is available. Therefore, it is necessary to establish the quantitative relationship between the microstructure information, including porosity, cracks and m phase, and thermal conductivity for the preparation of high performance TBCs.

In this manuscript, the effect of microstructure on the thermal conductivity of 8 wt % YSZ thermal barrier coatings (TBCs) is evaluated. Using scanning electron microscopy (SEM) and electron back-scattered diffraction (EBSD), cross-section morphological features such as pores, cracks, m-phase content and grain boundary density of the coated samples are studied, and a general relationship between the microstructure and thermal conductivity is developed.

2. Materials and Methods

2.1. Materials and Preparation

The Metco A-2000 atmospheric plasma spray equipment with a F4-MB plasma gun (Sulzer Metco AG, Switzerland) was used to deposit coatings on aluminum substrates (130 mm × 85 mm × 3 mm). The ceramic powder used for the top coating was commercially available ZrO_2–8 wt % Y_2O_3 (Shenyang Shihua Weifen Materials Co. Ltd., Shenyang, China). Figure 1 demonstrates the powder morphology and particle size of the raw material. The medium size (D50) of the powder was 50.9 μm. For all the measurements and characterizations, freestanding coatings were obtained by grinding the substrate away from the back side to a thickness of 100–300 μm and then bending the substrate on the edge of the coating carefully to detach the coating from it on the convex side. Thick free-standing coatings (about 1 mm) for thermal properties were deposited using different parameters, as summarized in Table 1. Prior to spraying, the aluminum alloy substrates (130 mm × 85 mm × 3 mm) were grit-blasted and degreased ultrasonically in acetone. During the spray process, compressed air was applied to both sides of the substrates to maintain identical cooling conditions, with both having approximately the same substrate temperature.

The in-flight parameters of velocity and temperature during the coating deposition on the substrate were measured by an online monitoring system (Spray Watch 2i, OSEIR, Tampere, Finland).
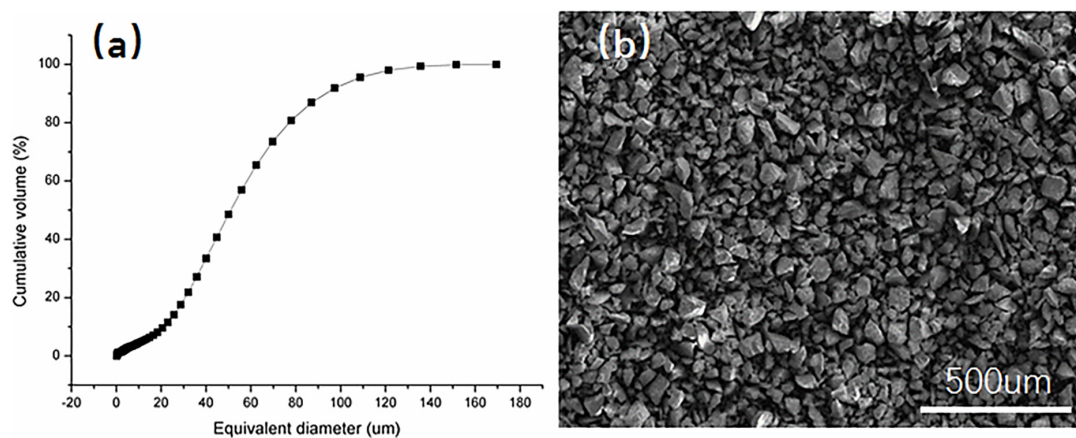
Figure 1. (**a**) Equivalent diameter distribution and (**b**) morphology of feeding powders.

Table 1. Plasma spray parameters and particle velocity, temperature.

Spraying Conditions	N1	N2	N3	N4	N5	N6	N7	N8	N9
Current (A)	550	550	550	600	600	600	650	650	650
Ar (L/min)	35	40	36	35	40	36	35	40	36
H_2 (L/min)	7	10	12	7	10	12	7	10	12
Velocity (m/s)	197	217	201	206	213	228	214	205	237
Temperature (°C)	2750	2931	2893	2835	3007	3221	2903	3079	3294

2.2. Microstructure Characterization

The microstructure of the TBCs was characterized qualitatively by microstructure observation and quantitatively by the Image Pro Plus (IPP, Image Pro Plus 6.0) technique by gray level variation. Pores appear very dark, and these were distinguished and quantified by image analysis. In this paper, the direct examination of the coating microstructures from cross-sections of the coatings using a scanning electron microscopy (SEM) provided comparative information about the porosity of different coatings. A SEM system (Magellan 400, FEI, Hillsboro, OR, USA) equipped with EBSD (INCA SERIES, Oxford Instrument, Oxford, UK) was used for this purpose. In conjunction with the EBSD detector, the phase composition and the information on the grain structures were shown in the microstructural images. The free-standing coatings were mechanically shaped into pieces (3 mm × 3 mm × 1 mm) and then polished by an ion milling system (Leica EM TIC 3X, Wetzlar, Germany). The backscattered images were employed for image analysis, automatic thresholds were used to distinguish between the pores and the ceramic matrix by the intensity of light from the other portions of the coatings. Ten images from different locations for each specimen at a magnification of 1500× were used for the quantitative measurement of all microstructure information.

Using the SEM-EBSD system for microstructure and phase composition analysis, the phases and grain size were studied by EBSD analysis. The Kikuchi patterns of different phases obtained by EBSD were different, so the m-phase could be easily distinguished from the other phases by EBSD. The m-phase content could be determined from its area fraction in EBSD mapping images. Ten EBSD mapping images from different locations for each specimen at a magnification of 1500× were acquired for the determination of the m-phase content. A phase with grain information map was constructed using the phase component in the software (Figure 2a,b). This map presents the phase distribution and grain information in the polished cross-section of the TBCs.
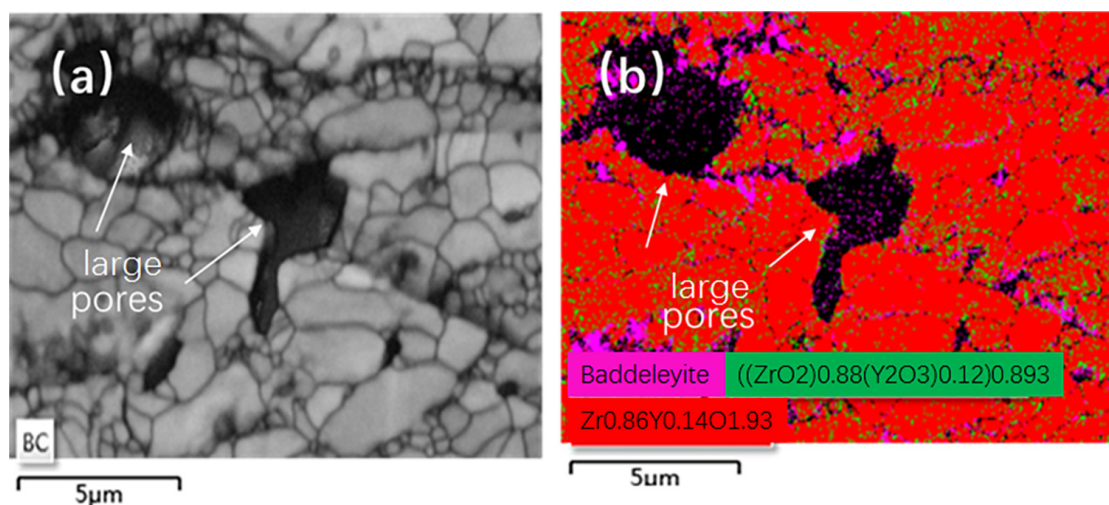
Figure 2. EBSD mappings of cross sections (**a**) grain boundary and (**b**) the phases distribution.

2.3. Thermal Conductivity Measurements

The TBCs were removed from the substrate and then polished into small diameters of 10 mm and 5 mm that could be used for thermal diffusion and specific heat capacity tests, respectively. The measurements of thermal diffusivity were performed by commercial laser flash equipment (TD-79A, SIC, Shanghai, China) from room temperature to 1200 °C. Specific heat capacity of the TBCs was tested according to the ASTME 1269-05 standard [22], using a diamond DSC (SIC) produced by Perkin Elmer (Waltham, MA, USA) over a temperature range from room temperature to 500 °C. Above 500 °C, the specific heat capacity was calculated by using the Neumann-Kopp law [23]. The density of coatings was determined using Archimedes' principle. Hence, the thermal conductivity can be calculated by the equation

$$\lambda = \alpha \rho C_p$$

where α, ρ and C_p are the thermal diffusivity, density and specific heat of the coatings, respectively.

3. Results and Discussion

3.1. Spray Parameters and Phase Content

The spray parameters, the temperature, and the velocity of particles during the deposition of the nine TBCs were listed in Table 1. The contents of m-phase and grain boundary density were shown in Table 2. The Ar and H_2 flow rates have great influence on the in-flight particles' velocity. Moreover, the particles' temperature might be closely related to the current and H_2 flow rate. Table 1 shows that the particles' velocity and temperature increases with increasing Ar and H_2 flow rates and increasing current. So, high current and H_2 flow rates could provide high energy to the particles and make the particles melt more extensively. It could be seen that the increase of current and H_2 was always accompanied by an increase of m-phase content, as shown in Table 2. The m-phase may be formed during the cooling process, and its content increases with increasing loss of yttrium due to vaporization during spraying at increasing particles' temperature. During the spray cooling process, t-phase was found to evolve through a martensitic transformation into m-phase at around 950 °C, resulting in a volume increase and promoting the increase of defects such as cracks and pores. In Figure 2a, the coating contains coarse grains (the grain size is 5 µm), columnar grains (aspect ratio >2), and a large number of small equiaxed grains (20–500 nm). It can be seen that the coatings were composed of large numbers of coarse and fine equiaxed grains, and only a small amount of columnar ones, which could be attributed to the low melting extent of in-flight particles [24]. If the size of the finest grain were smaller than three times the scanning step for acquiring EBSD maps, it could result in systematic errors caused by the EBSD resolution limit. Therefore, all such types of reading were discarded. Some of monoclinic phase grains were fine. This can be explained by the fact that t to m phase transformation usually occurs partly inside larger primary t grains, with the fine m-grains being subsequently developed [25]. The grain boundary density was inversely related to the grain size. With the decrease in grain size, the grain boundary density increases, as verified in Table 2.

Table 2. Coating parameters.

Coating Parameters	N1	N2	N3	N4	N5	N6	N7	N8	N9
Y_2O_3 Content (wt %)	7.85	7.78	7.71	7.68	7.73	7.65	7.46	7.38	7.31
m-ZrO_2 Content (%)	1.03	1.37	1.51	1.55	1.47	1.95	1.90	2.74	2.85
Grain Boundary Density(m/µm^2)	2.59	2.56	2.61	3.48	2.29	2.87	1.42	3.43	2.43

3.2. Microstructure of TBCs

Figure 3 displays the SEM image of thermal barrier coating by atmospheric plasma spraying. A variety of pores and cracks can be clearly distinguished. Therefore, the qualitative and quantitative analysis of the coatings' microstructure using SEM micrographs of mirror-polished cross-sections

was carried out. Through image analysis, the major axis "a" and minor axis "c" of every void in the microstructure, approximated as an ellipse, were measured to calculate the ratio a/c. If the ratio was <3, then the defect could be described as a pore; and if it was >3, then it could be considered as a crack. Furthermore, more meticulous work on the cracks was done, in which the angle and length of each crack were measured. The angle was that between the major axis of the crack and the direction of the coating/substrate interface. Hence, an angle of 0° indicates a crack parallel to the coating/substrate interface. Cracks forming an angle in the 0°–45° range were named small-angle cracks while those forming an angle of 45°–90° were referred as big-angle cracks. The length of cracks was determined by measuring the length of the major axis of the equivalent ellipse. The calculated length densities (length of cracks/μm^2) of the two kinds of crack were shown in Figure 4. Using the atmospheric plasma spray (APS) to heat the YSZ powder and then spray it on the substrates, the particles achieved high temperature and speed. It was found that the spraying process greatly influences the evolution of different phase contents. In Figure 2b, it was clear that the m-phase appears around the large pores and small-angle cracks. This was due to rapid cooling. The tetragonal phase transforms to monoclinic phase accompanied by volume change. When the pressure in the pores and cracks was minimal, the t-phase easily transforms to m-phase. But when the pressure inside the coating was too large to transform, then the monoclinic phase was mainly distributed around the pores and cracks. The transition from the t-phase to m-phase occurs with about 3–5 of volume expansion, and m-phase transforms to t-phase with about 7 of volume shrinkage. At about 950 °C, the t-phase therefore transforms to m-phase with a volume expansion of 3–5. The linear regression equation shows that the pores and cracks and the length density of small-angle cracks in the coating were strongly correlated with the spray parameters and the monoclinic phase content.

$$\text{Porosity (\%)} = 10.825 - 0.00014X_1 - 0.00042X_2 - 1.499X_3 \qquad R^2 = 0.90 \qquad (1)$$

$$\text{Crack-porosity (\%)} = 14.599 - 0.015816965X_1 - 0.001496453X_2 - 0.878686315X_3 \qquad R^2 = 0.79 \qquad (2)$$

$$\text{Length Density of Small-angle Cracks } (\mu m/\mu m^2)$$
$$= 0.215790122 - 0.000371226X_1 - 0.00000980847X_2 - 0.026043962X_3 \qquad R^2 = 0.91 \qquad (3)$$

$$\text{Length Density of Big-angle Cracks } (\mu m/\mu m^2)$$
$$= 0.049720041 + 0.000355754X_1 - 2.94618 \times 10^{-5}X_2 - 0.001130176X_3 \qquad R^2 = 0.27 \qquad (4)$$

where X_1 is the particle velocity, X_2 is the temperature of particles, and X_3 is the content of m-phase. Equations (1) and (2) show the effect of particle velocity, temperature and m-phase content on the porosity and crack-porosity, respectively. These indicate that that higher particles temperature and velocity result in a reduction of pores and cracks. This means that powders were melted more extensively, and then pores and cracks decrease with the increase in the particles' temperature. Equation (3) describes the parameters that determine the length density of small-angle cracks. There was no m-phase content near the large-angle cracks. During the cooling process, the volume change of t-phase to m-phase leads to further reduction in the pores and cracks. However, spray parameters have a small influence on the big-angle cracks. Equation (4) shows that, if R^2 was too small, the correlation between the length density of big-angle cracks and the parameters was very small. Since the generation of the length density of big-angle cracks in the spraying process results from the release of stress, the big-angle cracks are more random and smaller.
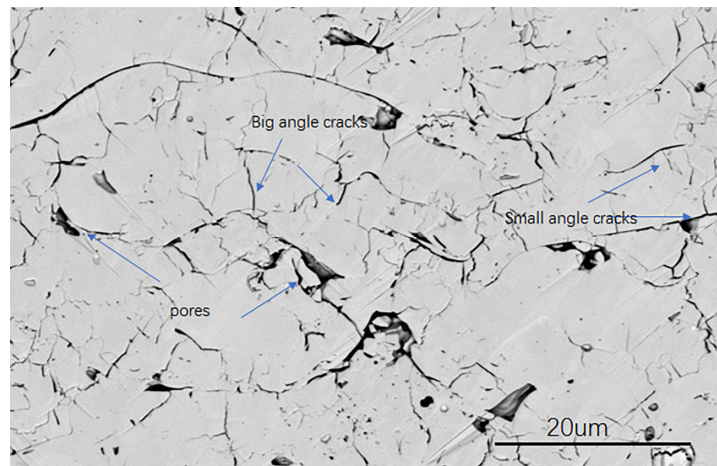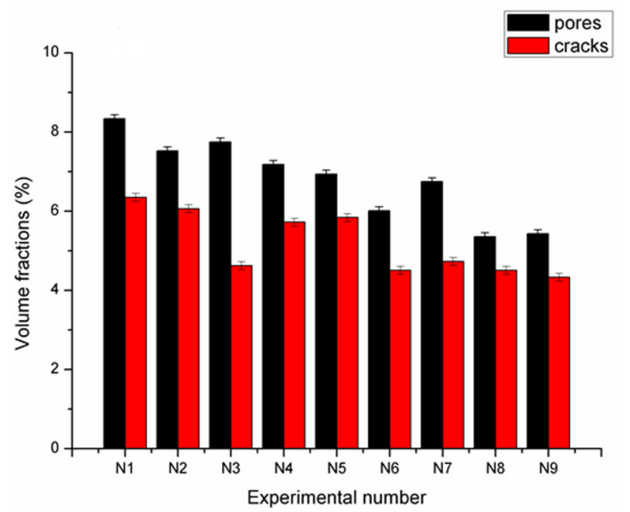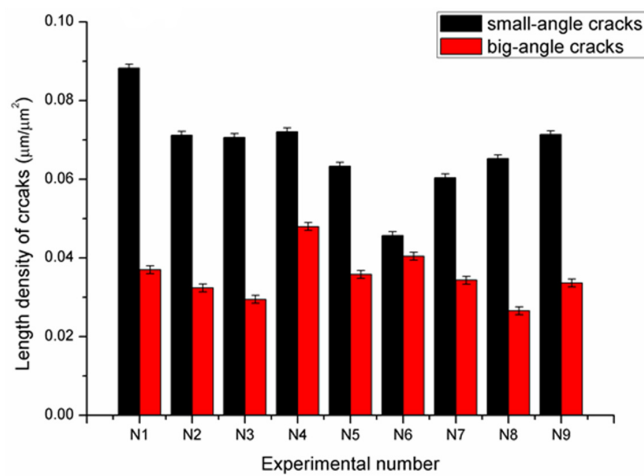
Figure 3. SEM image of polished cross-sections of APS N6 coating.

(**a**)

(**b**)

Figure 4. (**a**) Volume fractions of pores and cracks (**b**) length density of cracks.

3.3. Relationship between Microstructure and Thermal Conductivity

In Figure 5, the thermal conductivities of TBCs at room temperature and 1200 °C were compared. At 25 °C, the thermal conductivity was significantly higher than its value at 1200 °C. This can be explained by the phonon (lattice wave) conduction behavior. This was the interaction between phonons scattered by grain boundaries and point defects in the coating that causes their thermal conductivity to be inversely proportional to the temperature. In other words, an increase in the temperature leads to an increase in phonon scattering and a decrease in the thermal conductivity value [26]. The relationship between microstructure and thermal conductivity from the multiple regression equations at low and high temperature are given as follows:

Thermal Conductivity (room temperature)
$$= 1.79 - 0.104864402P - 0.038644461C - 0.009469272S + 23.24351385B - 0.170350528G \qquad R^2 = 0.82 \quad (5)$$

Thermal conductivity (1200 °C)
$$= 0.476267554 + 21.50434266B + 0.092513106M - 0.168259582G \qquad R^2 = 0.888 \quad (6)$$

where P is the porosity, C is the crack-porosity, S is the length density of small-angle crack, B is the length density of big-angle crack, and G is the grain boundary density.

In Equation (5), at low temperatures, pores, cracks, and the length density of small-angle cracks increase the phonon scattering, and effectively reduce the thermal conductivity. Moreover, more pores and cracks in the YSZ coatings might not have the decisive factor of reducing the thermal conductivity, suggesting that the other microstructural features also have significant influence on thermal conductivity. Grain boundaries were also one of the important sources of phonon scattering. The small grain size results in a large grain boundary density, which increases the intensity of phonon scattering, and thus leads to a lower thermal conductivity.

At high temperature (1200 °C), the average free path of the phonon decreases, and the mean free path of the phonon is close to several lattice spacings, so the larger the grain boundary density is, the stronger the phonon scattering will be. Furthermore, compared to the mean free path of the phonon (l_p) at high temperature, the pores are too large, and become rather ineffective scatterers. Thermal conductivity depends on l_p. Intense phonon collision leads to smaller l_p values with the increasing temperature. With the increasing temperature, the mean free path of phonons decreases from a value comparable with the grain diameter to the same order of magnitude as the lattice spacing. The mean free path of phonons at high temperature therefore reaches its lower limit (lattice spacing), which is far smaller than the micrometer-sized pores. Therefore, a pore has a weak scattering effect on the phonons at high temperature, and thus the effect of porosity at elevated temperature is negligible. m-phase has a significant effect at high temperature, and the point defect size is the same order of magnitude as lattice spacing. Therefore, in accordance with the previous discussion on the decrease of l_p with increasing temperature, while the scattering of phonons caused by point defects is negligible at low temperature, its influence is significant at high temperature. According to the defect reaction

$$\mathrm{Y_2O_3 \xrightarrow{ZrO_2} 2Y'_{Zr} + V''_0 + 3O^x_0}$$
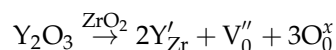
doping with a higher $\mathrm{Y_2O_3}$ content results in a higher point defect concentration. Since the m-$\mathrm{ZrO_2}$ contains a small amount of $\mathrm{Y_2O_3}$, it has the lowest point defect concentration; therefore, a coating with higher m-$\mathrm{ZrO_2}$ content would have higher thermal conductivity at elevated temperature. Consequently, the effect of m-$\mathrm{ZrO_2}$ content on thermal conductivity becomes vital at high temperature [27]. With the increase in m-phase content, the thermal conductivity of the coatings increases. In Equations (5) and (6), the length density of big-angle cracks has a large coefficient, meaning that it could strongly influence the thermal conductivity because, at both low and high temperature, heat can directly flow across the coating.
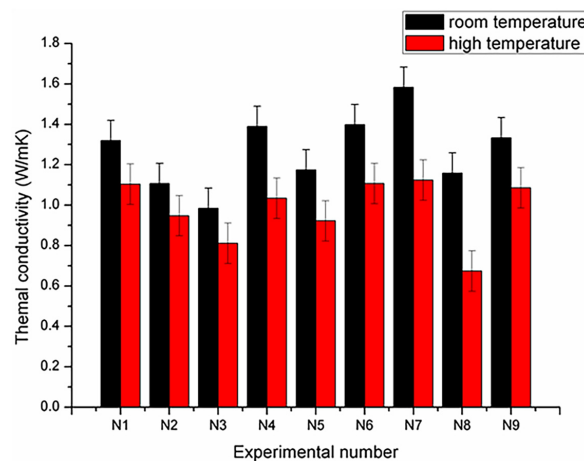
Figure 5. Thermal conductivity of APS coatings at 25 °C and 1200 °C.

4. Conclusions

- Spraying processes affect the m-phase contents of the coating, and increasing the current and the plasma gas flow rates will lead to an increase in the m-phase content.
- The volume change associated with the phase transition during the spraying process affects the microstructure of the coating. M-phase content and the in-flight particle state play significant roles in the formation of micro-morphology. The formation of big-angle cracks results from stress release, and their length density generally had very small and random variations with the process parameters.
- At low temperature (25 °C), pores, cracks (particularly the small-angle-cracks) and grain boundary density decrease the thermal conductivity, but the big-angle cracks increase the heat flow into the coating. At high temperatures (1200 °C), the effect of pores and cracks is negligible. The grain boundary density reduces the thermal conductivity. The effect of big-angle cracks on heat diffusion at both low and high temperatures is significant.

Author Contributions: Ningning Hu, Matiullah Khan, Yongzhe Wang, Xuemei Song, Chucheng Lin and Yi Zeng conceived and designed the experiments; Ningning Hu performed the experiments; Ningning Hu analyzed the data; Yongzhe Wang, Xuemei Song, Chengkang Chang, Chucheng Lin and Yi Zeng contributed materials and analysis tools; and Ningning Hu wrote the paper.

Conflicts of Interest: The authors declare no conflict of interest.

References

1. Feuerstein, A.; Knapp, J.; Taylor, T. Technical and economical aspects of current thermal barrier coating systems for gas turbine engines by thermal spray and EBPVD: A Review. *J. Therm. Spray Technol.* **2008**, *17*, 199–213. [CrossRef]
2. Liebert, C.H.; Stepka, F.S. Ceramic thermal barrier coatings for cooled turbines. *J. Aircr.* **2015**, *14*, 487–493. [CrossRef]
3. Osorio, J.D. Correlations between microstructure and mechanical properties of air plasma-sprayed thermal barrier coatings exposed to a high temperature. *J. Am. Ceram. Soc.* **2013**, *96*, 3901–3907. [CrossRef]
4. Lee, S.Y.; Kwon, J.Y.; Kang, T.W. Effects of thickness on thermal and mechanical properties of air-plasma sprayed thermal barrier coatings. *Mater. Sci. Forum* **2010**, *658*, 372–375. [CrossRef]

5.   Liu, H.; Jazi, H.R.S.; Bussmann, M. Experiments and modeling of rapid solidification of plasma-sprayed yttria-stabilized zirconia. *Acta Mater.* **2009**, *57*, 6013–6021. [CrossRef]

6.   Chi, W.; Sanjay, S.; Wang, H. Microstructure-thermal conductivity relationships for plasma-sprayed yttria-stabilized zirconia coatings. *J. Am. Ceram. Soc.* **2008**, *91*, 2636–2645. [CrossRef]

7.   Zhao, L.; Bai, Y.; Tang, J.J. Effect of particle in-flight behavior on the composition of thermal barrier coatings. *Appl. Surf. Sci.* **2013**, *286*, 184–191. [CrossRef]

8.   Cheng, D.; Xu, Q.; Lavernia, E.J. The effect of particle size and morphology on the in-flight behavior of particles during high-velocity oxyfuel thermal spraying. *Metall. Mater. Trans. B* **2001**, *32*, 525–535. [CrossRef]

9.   Vaßen, R.; Czech, N.; Malléner, W. Influence of impurity content and porosity of plasma-sprayed yttria-stabilized zirconia layers on the sintering behaviour. *Surf. Coat. Technol.* **2001**, *141*, 135–140. [CrossRef]

10. Arai, M.; Ochiai, H.; Suidzu, T. A novel low-thermal-conductivity plasma-sprayed thermal barrier coating controlled by large-pores. *Surf. Coat. Technol.* **2016**, *285*, 120–127. [CrossRef]

11. Song, X.; Liu, Z.; Suhonen, T. Effect of melting state on the thermal shock resistance and thermal conductivity of APS ZrO_2–7.5 wt % Y_2O_3, coatings. *Surf. Coat. Technol.* **2015**, *270*, 132–138. [CrossRef]

12. Wei, S.; Fu-chi, W.; Qun-Bo, F.; Zhuang, M. Effects of defects on the effective thermal conductivity of thermal barrier coatings. *Appl. Math. Model.* **2012**, *36*, 1995–2002. [CrossRef]

13. Raghavan, S.; Wang, H.; Dinwiddie, R.B. The effect of grain size, porosity and yttria content on the thermal conductivity of nanocrystalline zirconia. *Scr. Mater.* **1998**, *39*, 1119–1125. [CrossRef]

14. Dwivedi, G.; Wentz, T.; Sampath, S.; Nakamura, T. Assessing process and coating reliability through monitoring of process and design relevant coating properties. *J. Therm. Spray Technol.* **2010**, *19*, 695–712. [CrossRef]

15. Zhang, C. Effect of in-flight particle velocity on the performance of plasma-sprayed YSZ electrolyte coating for solid oxide fuel cells. *Surf. Coat. Technol.* **2008**, *202*, 2654–2660. [CrossRef]

16. Soyez, G.; Eastman, J.A.; Thompson, L.J. Grain-size-dependent thermal conductivity of nanocrystalline yttria-stabilized zirconia films grown by metal-organic chemical vapor deposition. *Appl. Phys. Lett.* **2000**, *77*, 1155–1157. [CrossRef]

17. Limarga, A.M.; Clarke, D.R. The grain size and temperature dependence of the thermal conductivity of polycrystalline, tetragonal yttria-stabilized zirconia. *Appl. Phys. Lett.* **2011**, *98*, 211906. [CrossRef]

18. Becher, P.F.; Swain, M.V. Grain-size-dependent transformation behavior in polycrystalline tetragonal zirconia. *J. Am. Ceram. Soc.* **2010**, *75*, 493–502. [CrossRef]

19. Ganvir, A.; Kumar, C.; Gupta, M.; Nylen, P. Thermal conductivity in suspension sprayed thermal barrier coatings: Modeling and experiments. *Therm. Spray Technol.* **2017**, *26*, 71–82. [CrossRef]

20. Wang, L.; Li, D.C.; Yang, J.S.; Shao, F.; Zhon, X.H. Modeling of thermal properties and failure of thermal barrier coatings with the use of finite element methods: A review. *J. Eur. Ceram. Soc.* **2016**, *36*, 1313–1331. [CrossRef]

21. Qiao, J.H.; Bolot, R.; Liao, H.; Bertrand, P. A 3D finite-difference model for the effective thermal conductivity of thermal barrier coatings produced by plasma spraying. *Int. J. Therm. Sci.* **2013**, *65*, 120–126. [CrossRef]

22. Fox, E.B.; Visser, A.E.; Bridges, N.J. Nanoparticle Enhanced Ionic Liquid Heat Transfer Fluids. U.S. Patent 20130068994 A1, 12 August 2014.

23. Touloukian, Y.S.; Bucco, E.H. *Thermophysical Properties of Matter—the TPRC Data Series. Volume 5. Specific Heat—Nonmetallic Solids*; Springer: New York, NY, USA, 1970.

24. Levi, C.G.; Hutchinson, J.W. Environmental degradation of thermal-barrier coatings by molten deposits. *MRS Bull.* **2012**, *37*, 932–941. [CrossRef]

25. Wang, Y.; Xu, F.; Gauvin, R. Growth modes for monoclinic yttria-stabilized zirconia during the martensitic transformation. *J. Am. Ceram. Soc.* **2017**, *100*, 4874–4883. [CrossRef]

26. Guo, H.B.; Vaben, R.; Stover, D. Atmospheric plasma sprayed thick thermal barrier coatings with high segmentation crack density. *Surf. Coat. Technol.* **2004**, *186*, 353–363. [CrossRef]

27. Chen, N.; Song, X.; Liu, Z. Quantitative analysis of the relationship between microstructures and thermal conductivity for YSZ coatings. *J. Therm. Spray Technol.* **2017**, *26*, 745–754. [CrossRef]